**33RD CONGRESS
OF THE INTERNATIONAL COUNCIL
OF THE AERONAUTICAL SCIENCES
STOCKHOLM, SWEDEN, 4–9 SEPTEMBER, 2022**

ICAS
2022
SWEDEN

VALIDATION OF A HYBRID LOADS OBSERVER FOR A SUBSCALE TEST AIRCRAFT WITH DISTRIBUTED ELECTRIC PROPULSION

Oliver Luderer[1] & Frank Thielecke[1]

[1]Hamburg University of Technology , Institute of Aircraft Systems Engineering , Neßpriel 5, 21129 Hamburg, Germany

Abstract

In this paper, a hybrid loads observer for the estimation of aircraft maneuver and gust loads is extended to account for propeller-wing-interaction induced loads using the subscale test aircraft *Wingfinity-BL* as an example. For this purpose, the results of the well-established program *XROTOR* are used as inputs of a simplified physically motivated interaction model. Subsequently, the model is corrected by linear terms to approximate the induced wing lift from preliminary wind tunnel experiments. The physical part of the loads observer is implemented as a Luenberger observer based on a low-fidelity non-linear flight dynamics model with strip aerodynamics and a structural loads model. It's physical basis allows for the simple integration of the derived interaction-model. Thereby, the use of low-fidelity models in the Luenberger observer offers the potential to significantly reduce the development time. However, this naturally increases the estimation error, as the validation with wind tunnel data shows. To account for the remaining error, a data-driven correction model is used based on the results of a 1-DOF wind tunnel test of a true to scale wing. It is shown that despite the use of low-fidelity models, a characteristically low complexity of the correction model can be realized within the hybrid observer. Moreover, the validation shows that a high accuracy of the loads estimation is still achieved. In a direct comparison with a purely data-driven observer, the advantages of the physical part in the hybrid observer become apparent, especially in the area of extrapolation.

Keywords: Distributed Propulsion, Hybrid Loads Observer, Loads Estimation, Propeller-Wing-Interaction

1 Introduction

By re-thinking the propulsion system and taking advantage of synergy effects between the propulsion and the aircraft structure, the emergence of distributed electric propulsion systems opens the design space for new, innovative aircraft configurations ([2],[4]). Besides potential system related advantages in the context of (hybrid) electric engine concepts, the increase in high-lift performance due to the interaction between the propulsion system and the wing is aimed to improve the overall aircraft performance, particularly in the low-speed range. On the downside, this interaction leads to pronounced non-elliptical lift curves in the vicinity of the propeller wake. At the same time, future aircraft tend to weight-optimized high aspect ratio wings to improve the aerodynamic efficiency. In particular, these weight-optimized structures in combination with the propeller induced forces and moments might lead to new load cases, which have to be considered not only in the aircraft design but also during its operation (e.g. optimize maintenance intervals, loads alleviation).

To efficiently monitor structural loads due to maneuver and gusts during the aircraft operation in real-time, a hybrid model-based observer method (hybrid loads observer) has been developed at the Institute of Aircraft Systems Engineering at the Hamburg University of Technology (TUHH) (e.g. [20]). The hybrid loads observer combines two state-of-the-art observer methods by correcting the loads estimation of a physics-based Luenberger observer [3] with a data-driven correction model based on the local-model network method [9]. Therein, the physical model is usually based on a high-fidelity flight dynamics model of the aircraft, which was derived by means of system identification leading to an expensive, time-consuming process.

However, for new, innovative aircraft configurations, high-fidelity flight dynamics models are hardly existing in the early stages due to the long and expensive development process. Therefore, the question naturally arises as to how far the fidelity of the physical model can be reduced while at the same time maintaining an efficient loads observer. To approach this question, in this paper a low-fidelity physical flight dynamics model of the subscale aircraft *Wingfinity-BL* (Fig. 1) is used that is parametrized based on aerodynamic calculations in LIFTING_LINE. Furthermore, former implementation of the hybrid observer ([20]) do not yet cover effects like the propeller-propeller-

Figure 1 – Aircraft model *Wingfinity-BL*

interaction and the interaction of the propulsion system with the wing (propeller-wing-interaction) accurately. Therefore, the physical model will be extended by a propeller-wing-interaction model derived from the results of an aerodynamic subroutine using XFOIL and XROTOR [19]. To this end, a simple, physically motivated interaction model based on the findings of Lemke [17] and Kreimeier [15] is implemented and presented in this paper. The data-driven correction model is derived from scenario based wind tunnel tests of a true to scale test aircraft wing with variable pitch control. To account for the reduction of physical model fidelity, the weight of the data-driven correction model is suitably increased compared to the reference work. The wind tunnel data is further used for the validation of the hybrid loads observer.

The paper is structured as follows: The hybrid loads observer structure is described in Sec. 2. The implementation of the non-linear flight dynamics model of the aircraft, propeller-wing-interaction model and structural loads model is presented in Sec. 3. Lastly, in Sec. 4 the design of the hybrid observer is depicted and the validation is performed.

2   Hybrid Loads Observer for Maneuver and Gust Loads Estimation

The hybrid loads observer combines two state-of-the-art loads observer methods and is fundamentally described in [20]. It includes a Luenberger observer [3], which is used for a physical a priori estimation of maneuver and gust loads using a nonlinear flight dynamics model of the aircraft and a data-driven correction model [9]. The correction model is based on the Local Model Network method to account for model inaccuracies and uncertainties. The general model structure of the hybrid loads observer is shown in Fig. 2.
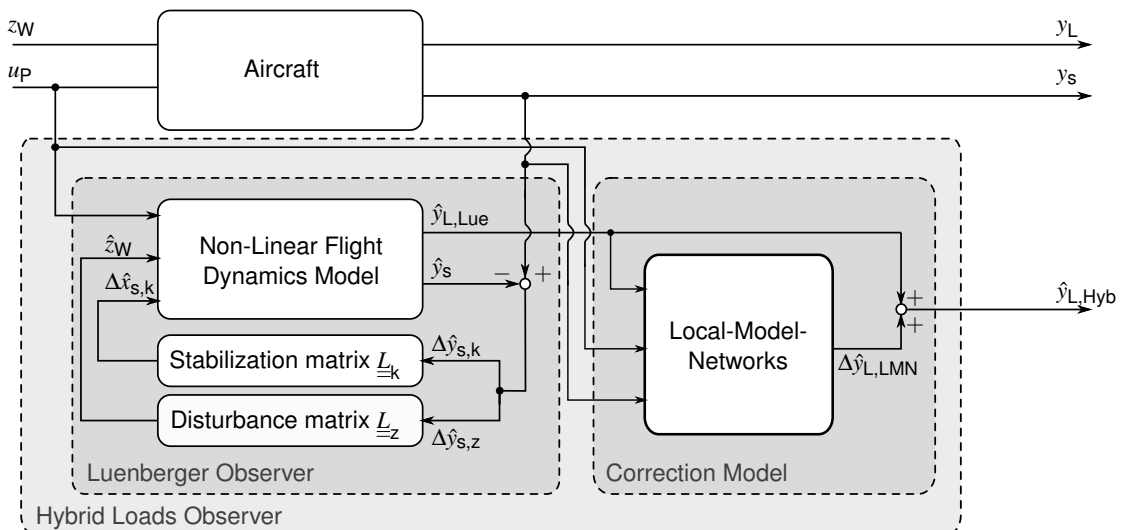

Figure 2 – Hybrid Loads Observer: Structure

The usage of a physical model in the hybrid observer enables easy integration of new physical effects, such as propeller-wing-interactions, and the calculation of structural loads $\hat{\underline{y}}_{\text{L,Lue}}$ for unknown maneuvers and high load events based on a physical structural loads model. Naturally, the accuracy of this physical loads estimation highly correlates with the underlying model accuracy, so that neglected physical effects or parameter uncertainties will lead to a prediction error. Previous work by Montel [20] has shown that by making use of high fidelity models, this prediction error can be minimized but the development is time-consuming and the prediction at high load factors remains challenging. Regarding this, his work has shown that the overall loads prediction accuracy could significantly be improved by correcting the estimated of the Luenberger observer by a data-based correction model derived from flight test data $\Delta\hat{\underline{y}}_{\text{L,LMN}}$. The resulting output equation of the hybrid loads observer can then be summarized according to Eq. 1.

$$\hat{\underline{y}}_{\text{L,Hyb}} = \hat{\underline{y}}_{\text{L,Lue}}(\underline{u}_{\text{P}}, \hat{\underline{x}}_{\text{s}}) + \Delta\hat{\underline{y}}_{\text{L,LMN}}(\underline{u}_{\text{P}}, \underline{y}_{\text{s}}, \hat{\underline{y}}_{\text{L,Lue}}) \tag{1}$$

2.1 Basic Loads Estimation (Luenberger Observer)

Compared to the open loop simulation of the loads, the Luenberger observer is characterized by an increased estimation accuracy due to state feedback of the aircraft state variables [3]. The simulated states $\hat{\underline{x}}_{\text{s,k}}$ are corrected continuously, such that model errors that integrate over time are reduced. In this way, parameter uncertainties can be compensated and the loads estimation is improved. Additionally, the feedback of $\Delta\hat{\underline{y}}_{\text{s,z}}$ allows the estimation of unknown disturbances, such as wind disturbances, which enables the estimation of local acting gust loads [21]. The state equation of the Luenberger observer is summarized in Eq. 2. Therein, $\Delta\underline{y}_{\text{s,z}}$ is the feedback for the disturbance estimation, $\Delta\underline{y}_{\text{s,k}}$ is the feedback for the model stabilization, $\hat{\underline{u}}_{\text{P}}$ are the pilot commands and $\underline{\underline{L}}_{\text{z}}$ and $\underline{\underline{L}}_{\text{k}}$ are the observer gain matrices, respectively.

$$\dot{\hat{\underline{x}}}_{\text{s}} = \begin{bmatrix} \dot{\hat{\underline{x}}}_{\text{s,k}} \\ \dot{\hat{\underline{x}}}_{\text{s,z}} \end{bmatrix} = f(\hat{\underline{x}}_{\text{s}}, \underline{u}_{\text{P}}) = \begin{bmatrix} \underline{\underline{L}}_{\text{k}} & 0 \\ 0 & \underline{\underline{L}}_{\text{z}} \end{bmatrix} \cdot \begin{bmatrix} \Delta\underline{y}_{\text{s,k}} \\ \Delta\underline{y}_{\text{s,z}} \end{bmatrix} = \begin{bmatrix} \underline{\underline{L}}_{\text{k}} & 0 \\ 0 & \underline{\underline{L}}_{\text{z}} \end{bmatrix} \cdot \begin{bmatrix} \underline{y}_{\text{s,k}} - \hat{\underline{y}}_{\text{s,k}} \\ \underline{y}_{\text{s,z}} - \hat{\underline{y}}_{\text{s,z}} \end{bmatrix}$$
$$\hat{\underline{y}} = \begin{bmatrix} \hat{\underline{y}}_{\text{s}} \\ \hat{\underline{y}}_{\text{L,Lue}} \end{bmatrix} = g(\hat{\underline{x}}_{\text{s}}, \underline{u}_{\text{P}}) \tag{2}$$

The compensation output vector $\underline{y}_{\text{s,k}}$ is presented in Eq. 3 and consists of the euler angles (Φ, Θ, Ψ), angular rates (p, q, r), body-fixed velocities (u, v, w) and altitude (H). The disturbance output vector $\underline{y}_{\text{s,z}}$ consists of the time derivatives of the body-fixed flight path velocities $(\dot{v}, \dot{w})$ and the time derivatives of the angular rates $(\dot{p}, \dot{q}, \dot{r})$. Jointly, they form the output vector of the measured aircraft motion $(\underline{y}_{\text{s}})$ and are continuously compared to their simulated equivalent $(\hat{\underline{y}}_{\text{s}})$ to ensure state feedback and disturbance estimation. The output vector of the Luenberger observer $(\hat{\underline{y}})$ is completed by the estimated component loads $\hat{\underline{y}}_{\text{L,Lue}}$ which are derived from the structural loads model of the aircraft (cf. Sec. 3.1).

$$\underline{y}_{\text{s,k}} = [\Phi, \Theta, \Psi, p, q, r, u, v, w, H], \qquad \underline{y}_{\text{s,z}} = [\dot{v}, \dot{w}, \dot{p}, \dot{q}, \dot{r}] \tag{3}$$

2.2 Loads Estimation Correction Model (Local-Model-Networks)

The local-model network method is a data-based modeling approach, which approximates complex relationships by weighted local-linear models (LLM) in simplified subspaces [11]. Both, parameters and the model structure, can be identified from flight test data. The model acts a MISO system which connects multiple inputs, e.g. pilot commands $\underline{u}_{\text{P}}$ or flight states $\underline{x}_{\text{s}}$, to a single output, e.g. loads output. This relationship is shown in Eq. 4 and Eq. 5, where the output $\Delta\hat{y}_{\text{L,LMN}}$ is approximated by a superposition of local linear functions $\Delta\hat{y}_{\text{L},i}$ depending on the input vector $\underline{u}_{\text{LMN}}$ and the corresponding parameter vector $\Theta^{(i)}$. The range of validity of each LLM is defined by a normalized weighting function w_i assuming a gaussian normal distribution with mean μ, a standard deviation σ and the property $\sum_{i=1}^{n} w_i = 1$ (cf. [9]). Due to a transparent model structure and the underlying local linear functions,

the structure of the local-model network allows for physical interpretation and specific adaptation [11]. In the past, it has already been shown that complex relationships, especially in the context of loads estimation, could be efficiently estimated using local model networks [9], [10], [11]. These properties of local model networks to efficiently model complex relationships between inputs and load outputs and their physical interpretability are therefore exploited in this work to compensate for the low-fidelity physical model, thereby further exploring the potential of the hybrid observer.
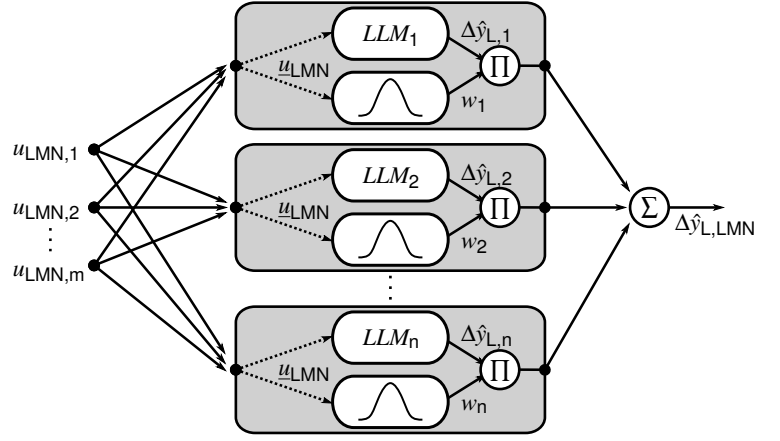

Figure 3 – Structure of a local model network

$$\Delta \hat{y}_{\mathrm{L,LMN}} = \sum_{i=1}^{n} w_i(\underline{u}_{\mathrm{LMN}}, \mu^{(i)}, \sigma^{(i)}) \cdot \Delta \hat{y}_{\mathrm{L},i}(\underline{u}_{\mathrm{LMN}}, \Theta^{(i)}) \tag{4}$$

$$\begin{aligned}
\Delta \hat{y}_{\mathrm{L},i}(\underline{u}_{\mathrm{LMN}}, \Theta^{(i)}) &= \Phi^T \cdot \Theta^{(i)} \\
&= \begin{bmatrix} 1 & u_{\mathrm{LMN},1} & \dots & u_{\mathrm{LMN,m}} \end{bmatrix}^T \cdot \Theta^{(i)} \\
&= \Theta_0^{(i)} + \Theta_1^{(i)} \cdot u_{\mathrm{LMN},1} + \dots + \Theta_{\mathrm{m}}^{(i)} \cdot u_{\mathrm{LMN,m}}
\end{aligned} \tag{5}$$

3   Non-linear Flight Dynamics Model: *Wingfinity-BL*

The presented hybrid loads observer is applied to the ATR-42 like aircraft configuration *Wingfinity-BL*, which was developed within the LuFo V-3 project ELASTIK (cf. Fig. 1). The subscale test aircraft is characterized by a distributed electric propulsion system with six propellers and a high aspect ratio wing ($\Lambda \approx 16$). It embodies a trade-off between current configurational trends of regional aircraft concepts that can be found in recent literature ([1], [2]) and serves as a development and validation platform of hybrid loads observer for future aircraft concepts. For the *Wingfinity-BL* a low-fidelity flight dynamics model has been modeled within the *ELASTIK* project. In essence, the model consists of quasi-stationary strip aerodynamics, whose theory and structure is presented in detail by Herrmann [12]. In contrast to the author's approach, the linear structural dynamics model is not enabled for the *Wingfinity-BL* and the aerodynamic model is parametrized using the LIFTING_LINE methodology [18] as a result of the in-house toolbox for preliminary design of subscale test aircraft *SCALAR* [19]. The flight dynamics model contains additional models from the in-house simulation library *FLYSIM*. This compromises specific models for equations of motion, actuator and control surface dynamics, an earth and atmosphere model (wind & turbulences) and a propulsion model that was parametrized in [19] using the analysis programs *XFOIL* [7] and *XROTOR* [8]. The non-linear model is completed by a structural loads model for the physical estimation of component loads (Sec. 3.1) and a propeller-wing-interaction model to account for effects regarding the interaction of the distributed propulsion system with the wing (Sec. 3.2).

3.1   Structural Loads Model

The modeling of the structural loads is based on a physical approach by [21], where the local loads at k pre-described load observation points ("LS") are determined by calculating the sum of effective forces and moments using the free-body principle. Additionally, the external as well as inertial forces and moments at j local section mass points ("MP") are taken into account. Gravity forces are not modeled since their contribution to the total local forces and moments is not represented in structural loads measurements due to calibration. Fig. 4 shows an exemplary distribution of mass points and load observation points on the right wing of the *Wingfinity-BL* and how the forces and moments at the i'th strip are related to the section mass point. Herein, external forces and moments are aerodynamic

($\underline{F}^{\mathrm{MP}_j}_{i,\mathrm{aero}}$) and propeller ($\underline{F}^{\mathrm{MP}_j}_{\mathrm{prop}}$) quantities.[1] Together with the inertial forces acting at the mass point ($\underline{F}^{\mathrm{MP}_j}_{\mathrm{inertia}}$), which are derived from the aircraft motion, the total force of the j'th mass point $\underline{F}^{\mathrm{MP}_j}$ results according to Eq. 6. The variables s_{start} and s_{end} indicate the starting and ending strip of a wing section.
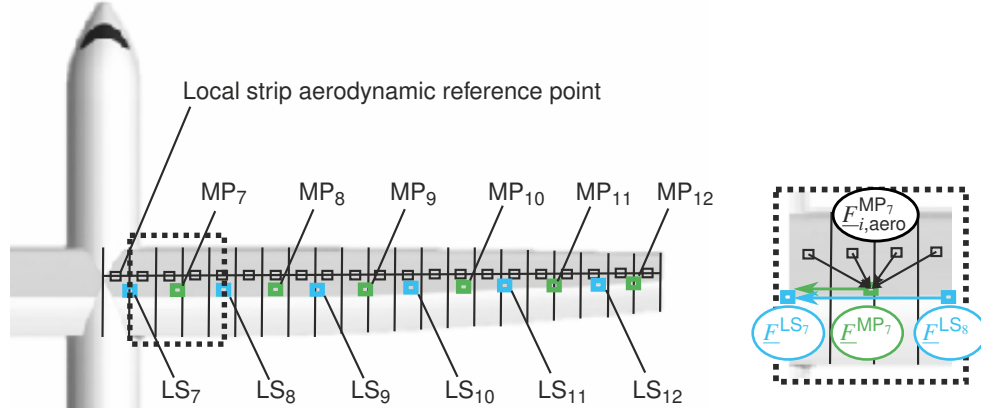
Figure 4 – Mapping of strip aerodynamic forces and moments on mass and loads observation points

$$
\begin{bmatrix} F_{\mathrm{xb}} \\ F_{\mathrm{yb}} \\ F_{\mathrm{zb}} \\ l_{\mathrm{b}} \\ m_{\mathrm{b}} \\ n_{\mathrm{b}} \end{bmatrix}^{\mathrm{MP}_j} = \underline{F}^{\mathrm{MP}_j} = \sum_{i=s_{\mathrm{start}}}^{s_{\mathrm{end}}} \underline{F}^{\mathrm{MP}_j}_{i,\mathrm{aero}} + \underline{F}^{\mathrm{MP}_j}_{\mathrm{prop}} - \underline{F}^{\mathrm{MP}_j}_{\mathrm{inertia}}
\tag{6}
$$

The forces and moments at the mass points are used to determine the component loads at the load observation points ($\underline{L}^{\mathrm{LS}_k}$) by using the transformation matrix $\underline{\underline{T}}_{\mathrm{LS}_k,\mathrm{MP}_j}$. Using the example of the right wing shown in Fig. 1, this relationship is described by Eq. 7, where k_{max} corresponds to the outermost load observation point LS_{12} and for k applies $k \in [7\ldots 12]$. For the *Wingfinity-BL*, 200 aerodynamic strips, 12 mass points and 12 load observation points were defined on the main wing. The parameterization is carried out in advance on the basis of analytical processes for determining the section mass and section centers of gravity.

$$
\underline{F}^{\mathrm{LS}_k} = \begin{bmatrix} \hat{Q}_{\mathrm{x}} \\ \hat{Q}_{\mathrm{y}} \\ \hat{Q}_{\mathrm{z}} \\ \hat{B}_{\mathrm{x}} \\ \hat{T}_{\mathrm{y}} \\ \hat{N}_{\mathrm{z}} \end{bmatrix}^{\mathrm{LS}_k} = \sum_{j=k}^{k_{\mathrm{max}}} \underline{\underline{T}}_{\mathrm{LS}_k,\mathrm{MP}_j} \cdot \underline{F}^{\mathrm{MP}_j}
\tag{7}
$$

3.2 Propeller-Wing-Interaction Model

Depending on the current propeller operating point (rotational speed, airflow velocity) and the current flight condition, the propeller induced velocities in the propeller wake of a tractor or puller configuration have a significant influence on the wing aerodynamics. This leads to a distinctive non-elliptical lift distribution in the affected wing area (cf. [24], [27]), also affecting the local component loads. Consequently, to consider these loads in the hybrid observer, the non-linear flight dynamics model has to be expanded by a propeller-wing-interaction model. In order to characterize the influence of the propeller-wing-interactions on the *Wingfinity-BL*, preliminary wind tunnel studies were carried out

---

[1]The influence of the propeller-wing-interaction model (Sec. 3.2) is included within the aerodynamic forces and moments.

in the past using a representative wing segment ([17], [19]). Based on the findings of the wind tunnel tests the following assumptions for the subscale test aircraft *Wingfinity-BL* can be made.

Assumption 1 *Propeller-wing-interactions are dominant only in the vicinity of the propeller slipstream. Therefore, the individual propellers can be considered as approximately isolated from each other.* [2]

Assumption 2 *Axial propeller induced velocities primarily lead to an increased effective dynamic pressure.*

Assumption 3 *Tangential propeller induced velocities primarily lead to a change in the local effective angles of attack.*

Taking these findings into account, a physically motivated propeller-wing interaction model can be derived, which is based on [15] and extends the model to a local spanwise formulation of the lift coefficient according to [17]. In the body-fixed coordinate system, the induced flow components acting on the i'th wing strip can be described by Eq. 8. The flow components $\bar{v}_{x,i}$, $\bar{v}_{y,i}$ and $\bar{v}_{z,i}$ are the corrected propeller induced velocities transformed from the propeller coordinate system into the body-fixed coordinate system. $\underline{\Omega}_{Ab} \times \underline{b}_{NP,i}$ forms the proportion of the additional flow velocities at the aerodynamic strips caused by the rotation of the aircraft $\underline{\Omega}_{Ab}$.

$$
\begin{bmatrix} u_{\text{eff},i} \\ v_{\text{eff},i} \\ w_{\text{eff},i} \end{bmatrix}_b = \begin{bmatrix} \bar{v}_{x,i} \\ \bar{v}_{y,i} \\ \bar{v}_{z,i} \end{bmatrix}_{Pb} + \begin{bmatrix} V_{TAS} \cdot \cos(\alpha) \\ 0 \\ V_{TAS} \cdot \sin(\alpha) \end{bmatrix}_{Ab} + \underline{\Omega}_{Ab} \times \underline{b}_{NP,i} \tag{8}
$$

The effective incident flow velocity $V_{\text{eff},i}$ in the propeller wake is then given by Eq. 9.

$$
V_{\text{eff},i} = \sqrt{\left(u_{\text{eff},i}^2 + v_{\text{eff},i}^2 + w_{\text{eff},i}^2\right)} \tag{9}
$$

From this equation, the factor of the effective increase of the dynamic pressure $(q_{\text{eff},i}/q_\infty)$ can be determined.

$$
\frac{q_{\text{eff},i}}{q_\infty} = \frac{V_{\text{eff},i}^2}{V_{TAS}^2} \tag{10}
$$

Analogously, the change of the effective local angles of attack in the propeller wake can be determined according to Eq. 11.

$$
\alpha_{\text{eff},i} = \arctan\left(\frac{w_{\text{eff},i}}{u_{\text{eff},i}}\right) \tag{11}
$$

A local non-dimensional lift coefficient distribution $C_{L,i}$ can then be formulated considering the spanwise zero lift coefficient of the i'th wing strip ($C_{L_0,i}$), the spanwise angle of attack dependent derivatives $C_{L_\alpha,i}$ and the sum of spanwise control surface derivatives $C_{L_{\delta_c}}$ of n_c control surfaces according to Eq. 12.

$$
C_{L,i} = \frac{q_{\text{eff},i}}{q_\infty} \cdot \left(C_{L_0,i} + C_{L_\alpha,i} \cdot \alpha_{\text{eff},i} + \sum_{c=1}^{n_c} C_{L_{\delta_c}} \cdot \delta_c\right) \tag{12}
$$

Fig. 5 shows the result of the propeller-wing-interaction model compared to measurement data recorded in the wind tunnel tests ([17] or [19]). During the campaign different flow velocities ($V = 10\,\mathrm{m s^{-1}}$, $13\,\mathrm{m s^{-1}}$, $16\,\mathrm{m s^{-1}}$), rotational speeds ($N = 5000\,\mathrm{min^{-1}}$, $6000\,\mathrm{min^{-1}}$, $7000\,\mathrm{min^{-1}}$) and angles of attack ($-3°$, $0°$, $3°$, $6°$) were considered. The comparison to the initial simulation results of the implemented interaction model reveal that the influence of the tangential induced velocity on the wing aerodynamics is clearly overestimated (cf. Fig. 5). This effect is addressed in various literature (e.g.

---

[2]This assumption is also consistent with de Vries [6], where a very similar experimental set-up with three leading-edge propellers was investigated in a wind tunnel test. The results have shown that the slipstreams of the distributed propulsion system rather remain as three independent streamtubes.

[27], [26], [13]) and might be explained by the reduction of the rotational energy in the propeller wake due to the presence of the wing, which is not considered by the interaction model. Since initial results from laboratory or wind tunnel tests are typically available at an early stage of development, the quality of the interaction model is subsequently initially improved on the basis of first results from the wind tunnel tests. Thus, a "swirl recovery factor" K_{SRF} is introduced to correct the tangential velocities $v_{\text{z},i}$.

$$\bar{v}_{\text{z},i} = v_{\text{z},i} \cdot (K_{\text{SRF}} + K_{\text{tan},\alpha} \cdot \alpha) \tag{13}$$

In order to additionally compensate for potential model errors regarding the axial propeller induced velocities $v_{\text{x},i}$, an additional correction factor (K_{ARF}) is applied according to Eq. 14. Furthermore, angle of attack dependent effects are taken into account by a linear correction in both equations ($K_{\text{ax},\alpha}$, $K_{\text{tan},\alpha}$).

$$\bar{v}_{\text{x},i} = v_{\text{x},i} \cdot (K_{\text{ARF}} + K_{\text{ax},\alpha} \cdot \alpha) \tag{14}$$

The introduced correction factors were identified with the in-house developed tool *DAVIS* using system identification techniques (cf. Tab. 1). Overall, a good agreement can be achieved, with slight deviations in the area of the propeller tips and the nacelle. The axial reduction factor (K_{ARF}) is close to one, which confirms the accuracy of the implemented propeller slipstream model in [19].
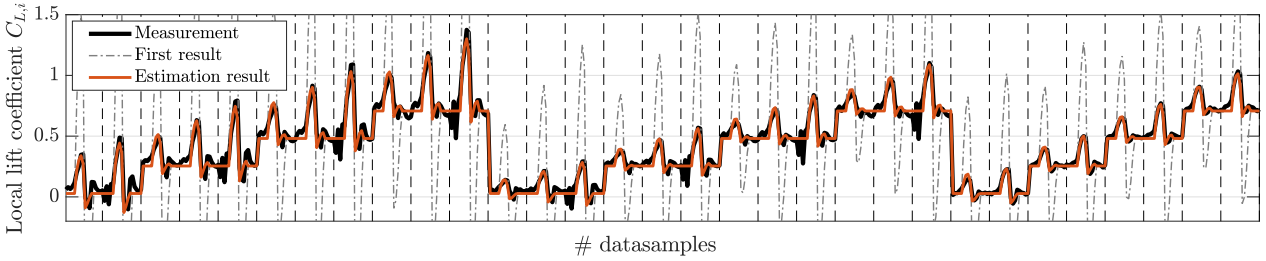

Figure 5 – Estimation result of the corrected propeller-wing-interaction model at various operating conditions (airflow velocity V, angle of attack α and rotational speed N)

Parameter	K_{ARF}	K_{SRF}	$K_{\text{ax},\alpha}$	$K_{\text{tan},\alpha}$
Estimated value	1.0023	0.1549	-2.0114	0.22056

Table 1 – Estimation result of the propeller-wing-interaction model correction factors

4   Hybrid Loads Observer Design and Validation

In the following, the non-linear flight dynamics model of the *Wingfinity-BL* is used to design the Luenberger observer as a part of the physical loads estimation in a model-based design approach (cf. Sec. 4.1). For the validation of the resulting loads estimation, a scenario-based wind tunnel test based on a 1-DOF wind tunnel wing is designed and presented in Sec. 4.2. Both, the loads estimation of the Luenberger observer and the results of the wind tunnel campaign are subsequently used to design the correction model for compensation of the remaining estimation errors. For this purpose, an adapted flight dynamics model is used taking into account the boundary conditions of the wind tunnel tests. Thereby, the model is simplified with regard to its equations of motion to one degree of freedom around the pitch axis. Lastly, the design of the correction model is carried out and the validation of the hybrid loads observer is performed. Due to limitations caused by missing input variables for the gust estimator in the wind tunnel setup (cf. Eq. 3), it was deactivated and not considered during the validation.

4.1   Design of the Luenberger Observer

The design of the Luenberger observer is based on a model-based design process using the non-linear flight dynamics model of the *Wingfinity-BL* and system identification techniques [21]. The

goal is to estimate the observer gain matrices $\underline{\underline{L}}_z$ and $\underline{\underline{L}}_k$. For this purpose, the aircraft in Fig. 2 is substituted by the non-linear flight dynamics model (reference model) exposed to noise processes (input, process and measurement noise). These will control the observer gain margins in analogy to the design of a kalman filter [21]. Therein, the choice of noise processes is crucial for the robustness of the Luenberger observer during operation. Increasing the input noise on the reference model increases the uncertainty of the observer model (design model) and consequently shifts the weighting within the observer towards the measurement data. This results in a larger gain of the state feedback ($\underline{\underline{L}}_k$). In contrast, an increase of the process noise (turbulence) at the reference model wind inputs results in larger gains of the disturbance feedback ($\underline{\underline{L}}_z$). Lastly, an increase in the measurement noise increases the uncertainty of the reference model, and therefore shifts the weighting within the observer towards the design model leading to smaller state feedback gains [20]. Thus, by choosing the magnitudes of the noise processes, the confidence level of the underlying observer model can be defined. To this end, all noise processes are modeled as a bandwidth-limited white noise.

Input noise σ_{u_P} The input noise represents a disturbance process that affects the pilot commands in the reference model. Due to the low-fidelity modeling approach, the overall model of the *Wingfinity-BL* is attributed rather a small confidence level, so that the standard deviation of the input noise σ_{u_P} of the control surfaces (only: ailerons, elevators and rudder) is conservatively set to $\Delta\phi = \pm 0.2°$. Additional noise ($\Delta\eta_{Fi} = \pm 0.35\%$) is applied to the commanded thrust lever of the engines to account for drag model uncertainties.

Measurement noise σ_{y_s} The magnitudes of the measurement noise are estimated from available measurement data at the institute based on representative hardware ([16], [23]). To ensure robustness against lateral model errors particularly against the background of the low-fidelity model, it is found in analogy to [21] that an increase of the noise intensity of the measurement value $\dot{r}_{Kb}$ by a factor of 20 is useful.

Process noise σ_W To simultaneously design the disturbance model, wind inputs are defined in the reference and design model at the wings and the vertical stabilizer. Process noise is applied to the inputs of the reference model based on the Dryden spectrum according to MIL-F-8785B (cf. [20], [5]). The standard deviation of the process noise is set to $10\,\mathrm{m\,s^{-1}}$ for the horizontal wind input at the vertical stabilizer ($v_{\mathrm{ff,Wb}}$). For the vertical wind inputs at the left (l) and right (r) wing ($w_{\mathrm{wl/r,Wb}}$) the standard deviation is $5\,\mathrm{m\,s^{-1}}$ at light turbulence levels.

Parameter	Estimated value
$K_{\Phi,\Phi}$	9.99
$K_{\Theta,\dot{\Theta}}$	9.98
$K_{\Psi,\dot{\Psi}}$	8.41
$K_{p,\dot{p}}$	13.07
$K_{q,\dot{q}}$	69.61
$K_{r,\dot{r}}$	57.58
$K_{u,\dot{u}}$	5.68
$K_{v,\dot{v}}$	1.91
$K_{w,\dot{w}}$	8.82
$K_{H,\dot{H}}$	1.00
$K_{\dot{v}_{vff},\ddot{v}_{ff}}$	29.45
$K_{\dot{w}_{wl/r},\ddot{w}_{wl/r}}$	16.50
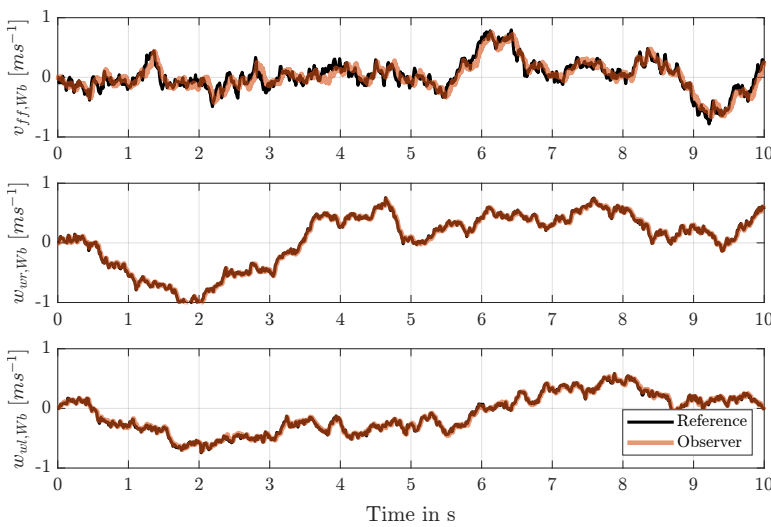
Figure 6 – Gust estimation of the disturbance model based on the estimated parameters in Tab. 2

Table 2 – Estimation result of the observer gains

The observer gain matrices of the state feedback and the disturbance model are estimated using the output error method and maximum likelihood principle within *DAVIS*. The goal of the estimation is to

achieve the best compromise between the competitive objectives of sufficient state feedback and sufficient gust estimation. Due to the low influence of the altitude in the operating range of subscale test aircraft, the state feedback of the altitude is kept constant to 1 during the entire estimation process. For the estimation, a ten-second maneuver in a trimmed, horizontal flight of the reference model is used. Within the process, the feedback gains are systematically increased to compensate for potential model inaccuracies of the non-linear flight dynamics model. The resulting estimated observer gains are summarized in Tab. 2. Fig. 6 shows that despite the deliberately introduced, increased measurement noise of $\dot{r}_{Kb}$ the accuracy of the lateral gust estimate $v_{ff,Wb}$ is satisfying. Nevertheless, it must be taken into account that due to the increased parameter uncertainties of the *Wingfinity-BL* model, higher deviations of the gust estimation can be expected during the observer operation.

4.2 Wind Tunnel Experiments for the Hybrid Loads Observer Design

For the design of the correction model a sufficient large and divers database is required. This database was generated in a 1-degree-of-freedom (1-DOF) wind tunnel experiment based on a true to scale *Wingfinity-BL* wing with variable pitch control. The measurement campaign comprises 534 individual scenarios (cf. Tab. 3) inspired by classic maneuvers for system identification ([9], [14] or [20]). Additionally, specific thrust maneuvers for preliminary investigations of the influence of the propeller-wing-interaction were performed at constant pitch angles, airspeeds, and flap positions. The set-up in the wind tunnel is shown in Fig. 7. Therein, the wing is clamped sidewise to the side wall of the wind tunnel. Due to the sliding bearing and actuation, the wing has a rotational degree of freedom around the pitch axis. Thereby, a dynamic adjustment of the angle of attack can be realized.

Type	# of Maneuvers	
	Training	Validation
ASM	8	78
FRD	6	66
ARD	7	84
ELD	2	22
SDA	15	142
THP	-	32
THD	-	48
HGR	4	42
Total quantity	**42**	**534**

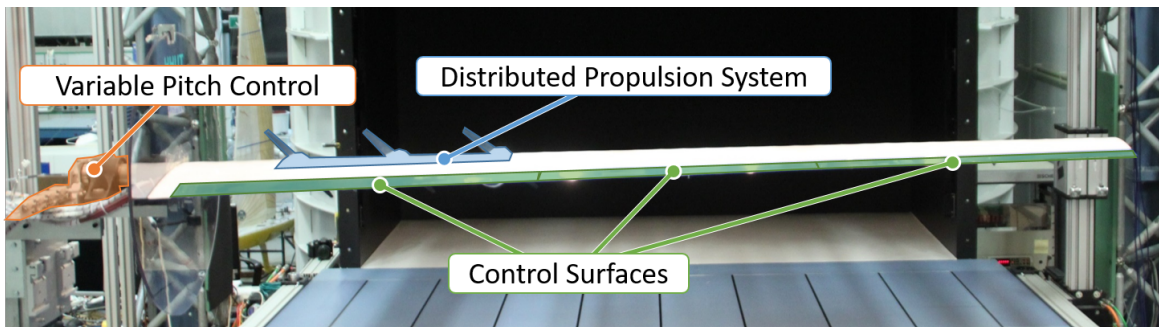Table 3 – Estimation and validation maneuvers of the measurement data

Figure 7 – Experimental set-up of the *Wingfinity-BL* test wing in the TUHH wind tunnel

The test wing has 3 control surfaces at the trailing edge (2 Flaps: η_{fR1}, η_{fR2} and 1 Aileron: ξ_R). In addition, the distributed propulsion system is located at the inner part of the wing where it is supposed to interact only with the innermost flap η_{fR1}. An end plate is used to approximate the effects due to the wing fuselage connection. In order to generate representative data sets, the individual scenarios of the wind tunnel tests are simulated and recorded in advance using a modified 1-DOF non-linear flight dynamics model of the *Wingfinity-BL*. The commanded flaps and thrust signals during the simulation, and the resulting angles of attack are used as inputs for the wind tunnel experiments. All maneuvers were performed in the airspeed range from $V = 16\,\mathrm{m\,s^{-1}}$ to $V = 25\,\mathrm{m\,s^{-1}}$ at varying flap positions. The propeller thrust levers are used symmetrically. The following maneuver types were considered: Thrust pulse (THP), Elevator- (ELD), Flap- (FRD), Aileron- (ARD) and Thrust-doublet (THD), 3-2-1-1 (ASM), Symmetric dynamic acceleration (SDA) and Quasi high-g roll maneuver (HGR) (cf. Tab. 3). All relevant measurement variables are acquired by a real-time measurement system from *dSPACE*. This includes calibrated strain gauges for recording the local loads, three revolution counter for the

propeller rotational speeds, four inertial measurement units for acceleration data, and wind tunnel-specific sensors. All related signals are summarized in Tab. 4. The sensor concept with regard to load observation points and acceleration sensors is shown in Fig. 8. The load sensor positioning is based on the idea to locally resolve for effects due to the propeller-wing-interaction at the innermost propeller. In contrast, the load observation point LS_4 is applied outside of the expected influence area of the distributed propulsion system, in order to separate the effects with and without the distributed propulsion system. All load observation points record the bending moment $B_{xb}^{LS_k}$, the shear force in z-coordinate direction $Q_{zb}^{LS_k}$ and the torsional moment $T_{yb}^{LS_k}$ in the body-fixed coordinate system. In addition, the shear force in thrust direction $Q_{xb}^{LS_k}$ is measured at LS_1. The strain gauges are applied on the wing beam and are connected as full bridges according to the principle of a Wheatstone bridge. They were calibrated during laboratory tests using the skopinski method [25].

Name	Symbol	Unit
Dynamic pressure	$\bar{q}$	Pa
Static pressure	p_s	Pa
Density	ρ	$kg\,m^{-3}$
Air temperature	T	K
Propeller rotational speed	$N^{1/2/3}$	min^{-1}
Angle of Attack	α	rad

Name	Symbol	Unit
x-Shear-Force	$Q_{xb}^{LS_1}$	N
z-Shear-Force	$Q_{zb}^{LS_{1/2/3/4}}$	N
Bending moment	$B_{xb}^{LS_{1/2/3/4}}$	Nm
Torsional moment	$T_{yb}^{LS_{1/2/3/4}}$	Nm
Acceleration	$a_{xb,yb,zb}^{MSB_{1/2/3/4}}$	$m\,s^{-2}$
Rotational speed	$\omega_{xb,yb,zb}^{MSB_{1/2/3/4}}$	s^{-1}

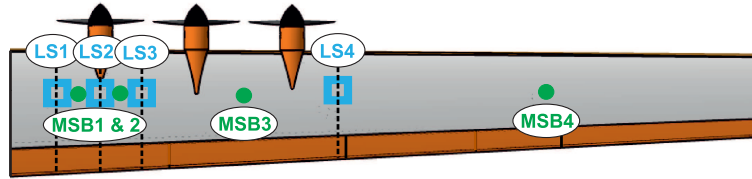Table 4 – Measurement variables of the wind tunnel experiments

Figure 8 – Sensor concept of the test wing. blue: Load observation points, green: Inertial measurement units (IMU)

4.3 Design of the Correction Model

In preparation for the design of the correction model in Sec. 4.3 the influence of the propeller-wing-interactions on the measured component loads is investigated at the load observation points LS_1 and LS_4. To this end, representative dynamic thrust maneuvers of the wind tunnel campaign are used. Each of these maneuvers is performed at different angles of attack ($\alpha = 0° - 6°$), airspeeds ($V_{TAS} = 15\,m\,s^{-1} - 25\,m\,s^{-1}$) and flap positions ($\eta_{fR1} = 0° - 10°$). All inputs were held constant during the test procedure of a single maneuver. The results of the investigation are shown in Fig. 9. In the figure $\Delta B_{xb}^{LS_x}$ and $\Delta T_{yb}^{LS_x}$ are the change of the measured load during the test with respect to the measured load at zero thrust lever. The study reveals that particularly LS_1 shows a significant correlation between the propeller rotational speed and the structural loads. For LS_4, which is located outboards of the propellers, no significant correlation is observed. This also retrospectively confirms the assumptions made in Sec. 3.2. Furthermore, the correlation strongly depends on the current operating point where particularly the flap deflections have a major impact on the bending moment increase and the direction of torsional moment change. This behavior is typical for propeller-wing interactions. Already present effects, such as the additional negative zero moment due to flap deflection, are amplified by the increase in dynamic pressure as a consequence of the propeller induced velocities. In this example, this consequently leads to a change in sign of the torsional moment change. Typically, due to the lower relative velocity increase in the propeller slipstream, the influence steadily decreases with

increasing airspeeds V_{TAS}. To summarize, the investigation shows the necessity of the propeller-wing interaction model for the estimation of structural loads in the vicinity of the propellers.
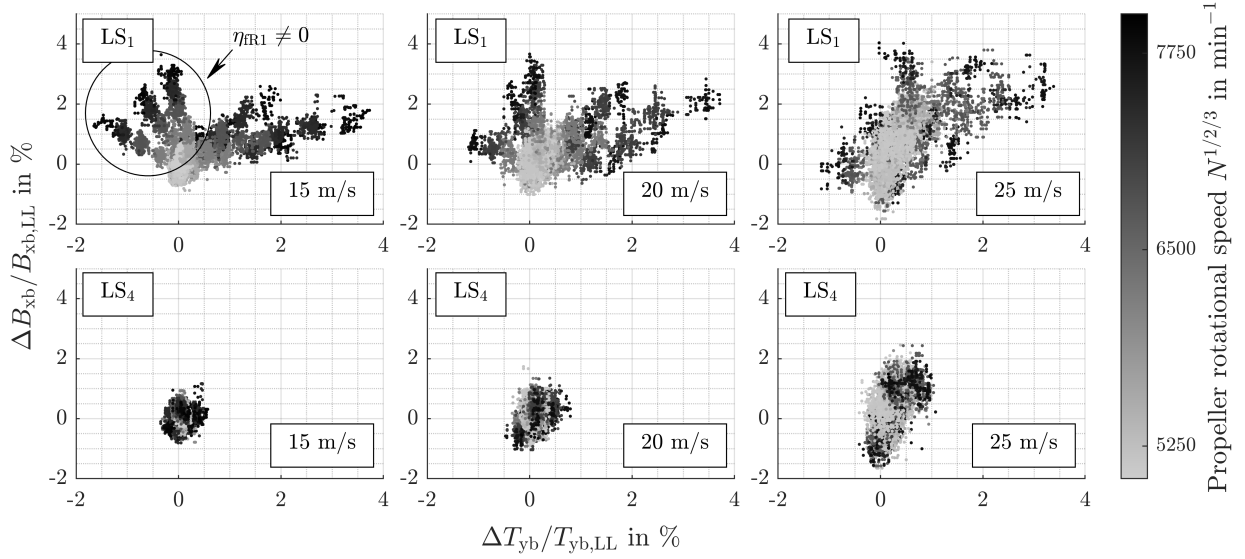

Figure 9 – Influence of propeller-wing-interactions on the change of component loads $\Delta B_{xb}^{LS_x}$ and $\Delta T_{yb}^{LS_x}$ at LS_1 and LS_4 at various operating points

The design of the data-driven correction model is performed using the *SIGMA* tool [9]. The commanded control inputs ($\underline{u}_P$) as well as the output variables measured during the wind tunnel tests ($\underline{y}_{s,k}$) serve as input variables of the local model network. In addition, the input vector is extended by the estimated component load of the Luenberger observer ($\hat{y}_{L,Lue}$) as it was proposed in [22]. Since the local-model-network method acts as a MISO system, an individual correction model has to be identified for each observed load output. Using the example of the bending moment at LS_1, the input vector results to Eq. 15. Note that, in difference to Eq. 3, the quantities u and w are combined to V_{TAS} and α via their kinematic relations. Further, the pitch angle Θ_{Kb} was neglected due to its correlation with the angle of attack in the wind tunnel set up. Lastly, all variables regarding the lateral motion are neglected.

$$\left[\underline{u}_P, \underline{y}_s, \hat{y}_{L,Lue}\right]^T = \left[\eta_{fR1}, \eta_{fR2}, \xi_R, V_{TAS}, \alpha, q_{Kb}, \dot{q}_{Kb}, N^{1/2/3}, \hat{B}_{x,Lue}^{LS_1}\right]^T \tag{15}$$

The input vector of LS_4 (cf. Eq. 16) is reduced by the control input of the innermost flap η_{fR1} since the load observation point is outside of the influence of the flap. Furthermore, based on the results of the preliminary investigations, relevant effects of the propeller-wing-interaction are not expected. Consequently, the propeller speeds $N^{1/2/3}$ are neglected, too.

$$\left[\underline{u}_P, \underline{y}_s, \hat{y}_{L,Lue}\right]^T = \left[\eta_{fR2}, \xi_R, V_{TAS}, \alpha, q_{Kb}, \dot{q}_{Kb}, \hat{B}_{x,Lue}^{LS_4}\right]^T \tag{16}$$

The correction model is used to correct the estimated loads of the Luenberger observer in the hybrid loads observer concept. To this end, the residuals between measured and a-priori estimated component loads are used as target criteria during the design of the correction model (cf. Eq. 17).

$$\Delta y_{L,LMN} = y_L - \hat{y}_{L,Lue} \tag{17}$$

The maneuvers selected for estimation, in terms of type and quantity, are summarized in Tab. 3. As it was shown during the preliminary investigations, the propulsion system induces noticeable component loads in the vicinity of the propeller wake depending on the current operating point. This results in a strong correlation over the input space. To address this aspect, a larger quantity of thrust maneuvers is considered in the estimation data set. In order to evaluate the extrapolation behavior of the hybrid loads observer, the maximum bending moment of the training data is restricted to $80\,\%$ Limit Load (LL). The structures of the local model network for load observation points LS_1 and LS_4

after the estimation are shown in Fig. 10. The required number of sub-models is $n_{\text{model}} = 5$ with a mean squared error of less than 2% limit load. Despite the simple low-fidelity physical modeling approach, a small number of sub-models is still required for the correction model. This feature is encouraging for further work, as the low complexity of the correction model was one of the key features of the hybrid load observer in preceding works [22]. However, compared to a high-fidelity physical model in [22], a slightly increased number of sub-models is needed.

(a) Bending moment $\Delta \hat{B}_{\text{xb}}^{\text{LS}_1}$

(b) Torsional moment $\Delta \hat{T}_{\text{yb}}^{\text{LS}_1}$
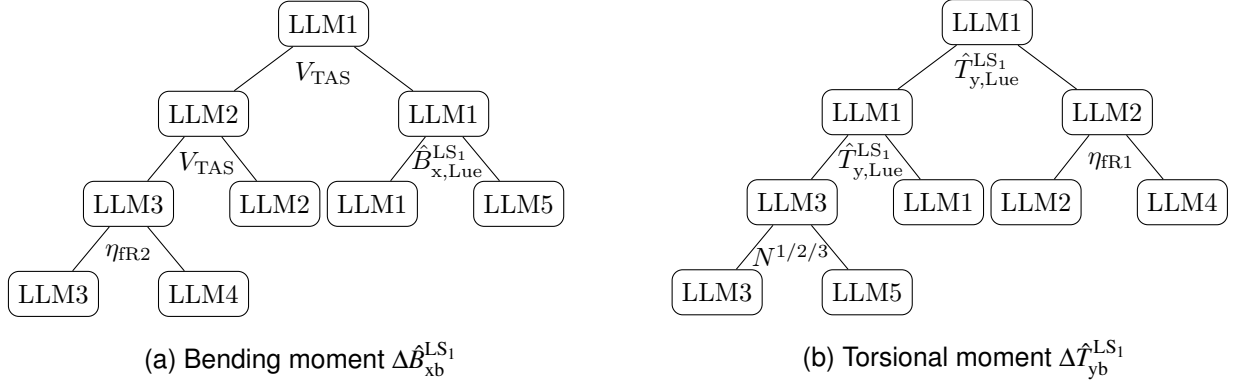
Figure 10 – Representation of the LMN structure as a model tree at LS_1 after the estimation

4.4   Validation of the Hybrid Loads Observer

The validation of the hybrid loads observer is carried out using the full measurement data base of 534 maneuvers (cf. Tab. 3). Fig. 11 shows qualitative results of the hybrid loads observer in the form of a correlation plot for the representative load observation points LS_1 and LS_4. Values in perfect agreement between measurement and simulation are located on the diagonal of the correlation plot. For comparison, the results of the Luenberger observer are also shown in the plots. They reveal model errors and parameter uncertainties in the loads estimation, leading to significant maximum deviations $\Delta_{\text{max}}|r|$ of up to 38% bending moment limit load or 29.4% in the measurement maximum. The standard deviation is $\sigma \approx 5\%$.
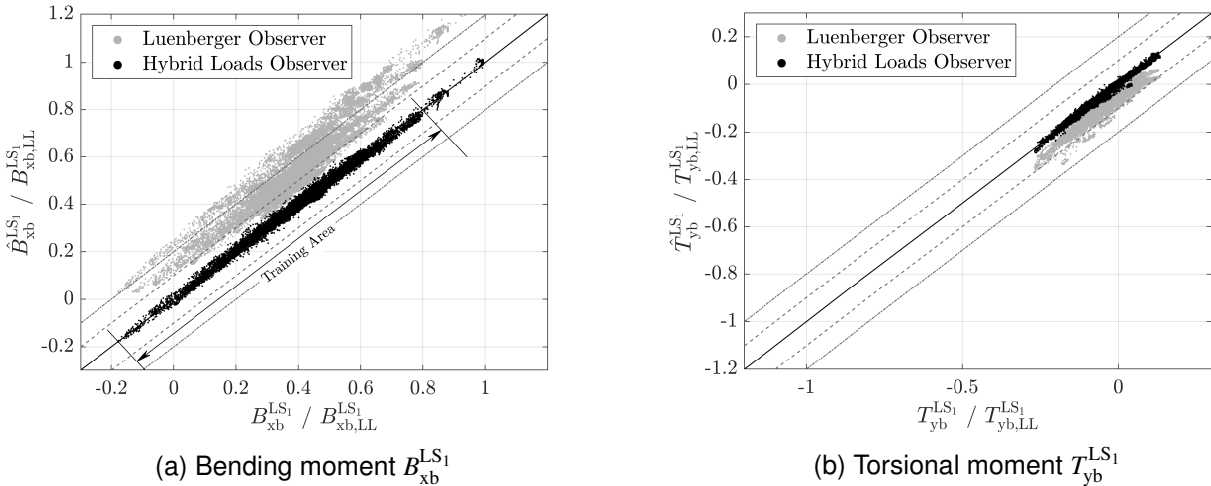

(a) Bending moment $B_{\text{xb}}^{\text{LS}_1}$

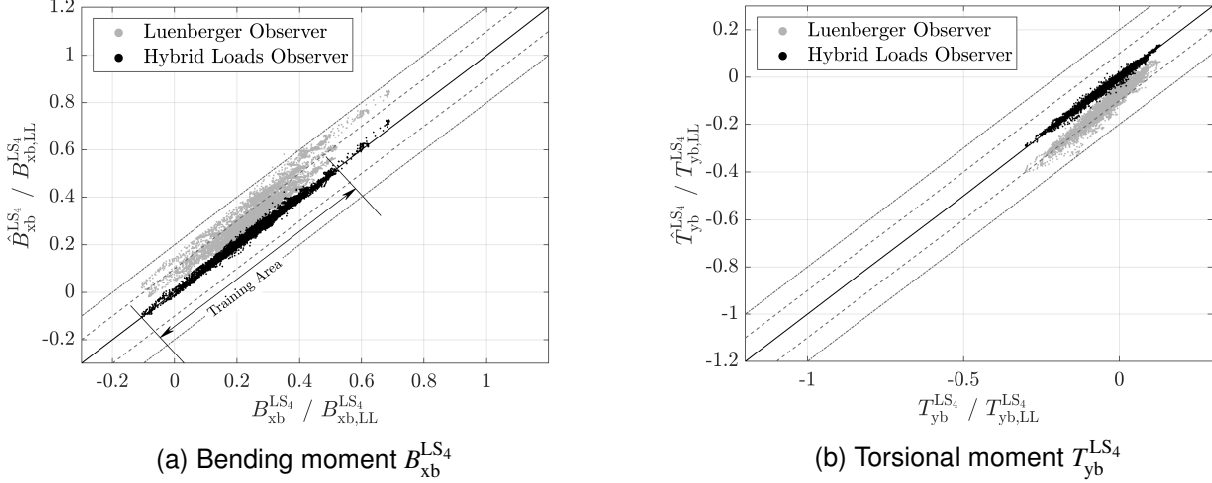(b) Torsional moment $T_{\text{yb}}^{\text{LS}_1}$

Figure 11 – Validation results of the Luenberger and hybrid observer at load observation point LS_1 normalized to the limit load and 10% (- - -) and 20% (-·-) tolerance bands

Fig. 11 illustrates that a significant improvement of the estimation accuracy can be achieved by extending the Luenberger observer to a hybrid loads observer. The estimation error in the maximum of the measured bending moment ($\Delta_{\text{max}}^{y_{\text{max}}}|r|$) is reduced from 29.4% to 0.5% Limit Load. This further highlights, that a high estimation accuracy can also be achieved in the extrapolation range ($> 80\%$ Limit Load). The equivalent estimation error of the torsional moment is reduced to 1.4% Limit Load.

The standard deviation of the considered load cases is below $1.0\,\%$ which underlines a good estimation result of the hybrid loads observer. Fig. 12 shows the results for load observation point LS_4, which are qualitatively comparable to LS_1. Higher deviations in the extrapolation area of the observer are noticeable which is reasoned by generally lower load levels in the outer wing sections [22]. In addition, the test wing has a low torsional stiffness, such that an increased wing twist is expected at high load levels in these wing sections. Since the structural dynamics model is neglected in the physical model of the observer and high load maneuvers were not used during the training of the local model network, a decreased loads estimation accuracy can be expected.

(a) Bending moment $B_{xb}^{LS_4}$

(b) Torsional moment $T_{yb}^{LS_4}$

Figure 12 – Validation results of the Luenberger and hybrid observer at load observation point LS_4 normalized to the limit load and 10% (- - -) and 20% (-·-) tolerance bands

The basic ideas for using simplified physical models in the hybrid observer are to reduce the development time on the one hand, but to provide basic physical relationships on the other hand. These are supposed to improve the loads estimation accuracy compared to the pure data-driven method particularly in the extrapolation area. In this context, Fig. 13 compares the results of the hybrid loads observer to the results of the pure local-model network with respect to the bending moment at LS_1. For this purpose, the method of local model networks is used to develop a virtual load sensor according to [9] or [20]. The design is based on the same input data as the hybrid observer (cf. Tab. 3). However, naturally the estimated load of the Luenberger observer is neglected in the input vector (Eq. 18). The required number of sub-models is $n_{model} = 8$.

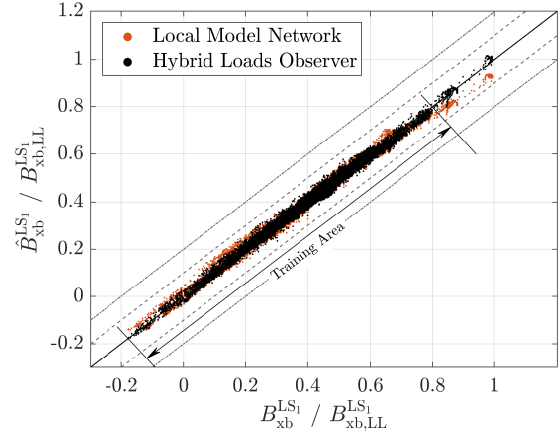Figure 13 – Comparison of hybrid loads observer and local model network results

$$\left[\underline{u}_P, \underline{y}_s\right]^T = \left[\eta_{fR1}, \eta_{fR2}, \xi_R, V_{TAS}, \alpha, q_{Kb}, \dot{q}_{Kb}, N^{1/2/3}\right]^T \tag{18}$$

The comparison shows that the hybrid observer approach is superior to the data-driven method in terms of accuracy in wide areas, which is especially true in the extrapolation area. This property of the hybrid loads observer was already shown in [20]. What is striking here, however, is that this property occurs despite the chosen low-fidelity modeling approach. The increased accuracy suggest that the provided basic physical relationships in the Luenberger observer enables a more targeted learning of plausible correction models and thus supports the estimation results of the hybrid loads observer. Moreover, the physical model also offers other typical advantages, such as good

13

interpretability and the possibility of drawing conclusions about potential model uncertainties on the basis of the correction model, which might be helpful in early design phases. The presented results provide first answers to the initial question of how far the physical part can be reduced in the hybrid observer concept. The results clearly show that despite the use of low-fidelity models, accurate loads estimation is still possible. Thereby, the presented study provides a good basis for potential further work, where the model complexity and the parameter accuracy might be further reduced.

5 Conclusion

In this work, a hybrid loads observer is designed for a subscale test aircraft with distributed electric propulsion and reduced fidelity of the physical model. For this purpose, a low-fidelity flight dynamics model and a simplified propeller-wing interaction model are used. They are parametrized using the aerodynamic analysis tools *XFOIL*, *XROTOR* and *LIFTING_LINE* and additional analytical analysis processes for parametrization of the structural loads model. Based on the derived physical model, the design of the Luenberger observer is carried out in a model-based design process and the correction model is derived from a scenario-based 1-DOF wind tunnel test. The validation shows that despite the reduction of physical model fidelity, a precise loads estimation is achieved through the higher weighting of the data-driven correction model. Moreover, a characteristic low complexity of only 5 sub-models is maintained. The results also show that a good estimation result can still be obtained in the extrapolation range, which is one of the main advantages of the hybrid load observer concept. It should be noted that the present study focused primarily on the influence of the propeller-wing-interaction and considered only the longitudinal motion in a simplified wind tunnel setup. However, the good-natured behavior in the design of the hybrid loads observer suggests that the results can potentially be transferred to real flight tests with all 6 degrees of freedom in possible future work.

6 Contact Author Email Address

mailto: oliver.luderer@tuhh.de, frank.thielecke@tuhh.de

7 Copyright Statement

8 Acknowledgement

References

[1] Airbus SE. *These pods could provide a blueprint for future hydrogen aircraft*. 2020. URL: https://www.airbus.com/en/newsroom/stories/2020-12-these-pods-could-provide-a-blueprint-for-future-hydrogen-aircraft (visited on 05/03/2022).

[2] Atanasov G., Silberhorn D., et al. "Short Medium Range Turboprop-Powered Aircraft as an Enabler for Low Climate Impact". In: *Deutscher Luft- und Raumfahrtkongress DLRK*. 2021. URL: https://elib.dlr.de/148094/ (visited on 05/03/2022).

[3] Bensch L., Henrichfreise H., et al. "Method for reconstructing gusts an structural loads at aircraft, in particular passenger aircraft". Pat. WO2007065659A1. 2007.

[4] Borer N. K., Patterson M. D., et al. "Design and performance of the NASA SCEPTOR distributed electric propulsion flight demonstrator". In: *16th AIAA Aviation Technology, Integration, and Operations Conference*. 2016, p. 3920.

[5] Chalk C. R., Neal T. P., et al. "Background Information and User Guide for Mil-F-8785B (ASG), 'Military Specification-Flying Qualities of Piloted Airplanes'". In: CORNELL AERONAUTICAL LAB INC BUFFALO NY, 1969.

[6] de Vries R., van Arnhem N., et al. "Aerodynamic interaction between propellers of a distributed-propulsion system in forward flight". In: *Aerospace Science and Technology* 118.10 (2021), p. 107009. ISSN: 12709638. DOI: 10.1016/j.ast.2021.107009.

[7] Drela M. "XFOIL: An Analysis and Design System for Low Reynolds Number Airfoils". In: *Lecture Notes in Engineering*. Springer Berlin Heidelberg, 1989, pp. 1–12. DOI: 10.1007/978-3-642-84010-4_1.

[8] Drela M. and Youngren H. *XROTOR*. URL: http://web.mit.edu/drela/Public/web/xrotor/ (visited on 05/03/2022).

[9] Halle M. "Lokalmodell-Netz-Identifikation als Analyse- und Bewertungsmethodik von Flugmanoeverlasten". Schriftenreihe Flugzeug-Systemtechnik. PhD thesis. Technische Universität Hamburg, Jan. 2016. ISBN: 978-3-8440-4306-8.

[10] Halle M. and Thielecke F. "Flight loads estimation using local model networks". In: *29th Congress of the International Council of the Aeronautical Sciences ICAS*. St. Petersburg, Russia, 2014.

[11] Halle M. and Thielecke F. "Local model networks applied to flight loads estimation". In: *31st Congress of the International Council of the Aeronautical Sciences ICAS*. Belo Horizonte, Brazil, 2018.

[12] Herrmann B., Theis J., and Thielecke F. "System Identification of a Nonlinear UAV Model with Distributed Aerodynamics and Flexible Structure". In: *6th Conference on Guidance, Navigation and Control CEAS*. 2022.

[13] Herzog N., Reeh A., et al. "Analysis of Distributed Electric Propulsion on Commuter Aircraft". In: *AIAA Scitech 2021 Forum*. Reston, Virginia: American Institute of Aeronautics and Astronautics, 2021. ISBN: 978-1-62410-609-5. DOI: 10.2514/6.2021-1199.

[14] Jategaonkar R. V. *Flight Vehicle System Identification: A Time-Domain Methodology, Second Edition*. Vol. 82. Reston, VA: American Institute of Aeronautics and Astronautics, Inc, 2015. ISBN: 978-1-62410-278-3. DOI: 10.2514/4.102790.

[15] Kreimeier M. "Evaluation of on-demand air mobility concepts with utilization of electric powered small aircraft". PhD thesis. RWTH Aachen University, 2018. DOI: 10.18154/RWTH-2018-223676.

[16] Krings M., Annighofer B., and Thielecke F. "ULTRA - Unmanned Low-cost Testing Research Aircraft". In: *2013 American Control Conference*. IEEE, 2013, pp. 1472–1477. ISBN: 978-1-4799-0178-4. DOI: 10.1109/ACC.2013.6580044.

[17] Lemke L., Luderer O., et al. "Aerodynamische Analyse verteilter Antriebe an einem Flügelsegment eines hochgestreckten Flügels". In: *Deutscher Luft- und Raumfahrtkongress DLRK*. Bremen, Germany, Sept. 2019. DOI: 10.25967/490115.

[18] Liersch C. and Wunderlich T. "A Fast Aerodynamic Tool for Preliminary Aircraft Design". In: *Multidisciplinary Analysis and Optimization Conference*. American Institute of Aeronautics and Astronautics, 2008. DOI: 10.2514/6.2008-5901.

[19] Luderer O., Jünemann M., and Thielecke F. "Validation of an Aerodynamic Model for the Analysis of Subscale Test Aircraft with Distributed Electrical Propulsion". In: *32nd Congress of the International Council of the Aeronautical Sciences ICAS*. Shanghai, China, 2021. ISBN: 9783932182914.

[20] Montel M. "Hybride Beobachter-Methode zur Strukturlastüberwachung und deren Validierung mit Flugversuchsdaten". Schriftenreihe Flugzeug-Systemtechnik. PhD thesis. Technische Universität Hamburg, Mar. 2018. ISBN: 978-3-8440-6354-7.

[21] Montel M. and Thielecke F. "Validation of a Model Based Structural Loads Monitoring System using the Flight Test Aircraft UW-9 Sprint". In: *AIAA Atmospheric Flight Mechanics Conference*. Reston, Virginia: American Institute of Aeronautics and Astronautics, 2015, p. 321. ISBN: 978-1-62410-358-2. DOI: `10.2514/6.2015-2237`.

[22] Montel M. and Thielecke F. "Validation of a hybrid observer method for flight loads estimation". In: *31st Congress of the International Council of the Aeronautical Sciences ICAS*. Belo Horizonte, Brasil, 2018.

[23] Sedlmair N., Theis J., and Thielecke F. "Flight Testing Automatic Landing Control for Unmanned Aircraft Including Curved Approaches". In: *Journal of Guidance, Control, and Dynamics* 45.4 (2022), pp. 726–739. DOI: `10.2514/1.G005917`.

[24] Sinnige T., van Arnhem N., et al. "Wingtip-Mounted Propellers: Aerodynamic Analysis of Interaction Effects and Comparison with Conventional Layout". In: *Journal of Aircraft* 56.1 (2019), pp. 295–312. ISSN: 0021-8669. DOI: `10.2514/1.C034978`.

[25] Skopinski T. H., Aiken W. S., et al. *Calibration of Strain-gage Installations in Aircraft Structures for the Measurement of Flight Loads*. NACA R-1178. National Advisory Committee for Aeronautics, 1953.

[26] Veldhuis L. L. M. "Review of propeller-wing aerodynamic interference". In: *24th Congress of the International Council of the Aeronautical Sciences ICAS*. Yokohama, Japan, 2004. ISBN: 0953399168.

[27] Veldhuis L. L. M. "Propeller Wing Aerodynamic Interference". PhD thesis. Delft University of Technology, 2005. ISBN: 90-9019537-8.